UC Berkeley
UC Berkeley Previously Published Works

Title

Visualizing coherent vibrational motion in the molecular iodine B3Π0+u state using ultrafast XUV transient-absorption spectroscopy

Permalink

Journal

ISSN

Authors

Poullain, Sonia M
Kobayashi, Yuki
Chang, Kristina F
et al.

Publication Date

DOI

Visualizing coherent vibrational motion in the molecular iodine $B\,^3\Pi_{0^+_u}$ state using ultrafast XUV transient-absorption spectroscopy

Sonia M. Poullain [1,2,*] Yuki Kobayashi [1,†] Kristina F. Chang [1] and Stephen R. Leone [1,3,4,‡]

[1]*Department of Chemistry, University of California, Berkeley, California 94720, USA*
[2]*Departamento de Química Física, Facultad de Ciencias Químicas, Universidad Complutense de Madrid, 28040 Madrid, Spain*
[3]*Chemical Sciences Division, Lawrence Berkeley National Laboratory, Berkeley, California 94720, USA*
[4]*Department of Physics, University of California, Berkeley, California 94720, USA*

Attosecond probing of core-level electronic transitions in molecules provides a sensitive tool for real-time observation of chemical dynamics. Here, we employ ultrafast extreme-ultraviolet (XUV) transient-absorption spectroscopy to investigate the excited state electronic and nuclear dynamics in a prototype molecule, I_2. A few-femtosecond visible pump pulse is employed to excite the I_2 molecule and an attosecond XUV pulse is used to probe the dynamics through iodine-$4d$ core-to-valence transitions. A highly extended vibrational wave packet ($v' = 10$–50, $v'_{\max} = 25$) is prepared by one-photon absorption in the valence excited $B\,^3\Pi_{0^+_u}$ state of I_2 and its motion is directly mapped due to the strong shift of the XUV core-level transition with internuclear separation. Through the imaging of this vibrational motion, we directly reconstruct the transition energy between the valence and the core-excited states as a function of internuclear distance. Besides single-photon dynamics, distinct direct dissociation pathways arising from two-photon pump absorption are also revealed.

I. INTRODUCTION

Ultrafast light sources in the attosecond time regime (from tens of attoseconds up to a few femtoseconds) from both large-scale facilities such as free-electron lasers and table-top experiments using high-order harmonic generation, are characterized by the unique power to resolve the electronic dynamics in molecules. Recent examples include measured time delays in the photoionization of ethyl iodide [1] and reported charge migration in iodoacetylene [2]. In this context, ultrafast extreme-ultraviolet (XUV) transient-absorption spectroscopy, characterized by excellent spectral and temporal resolution, has been shown to be an ideal tool to unravel the ultrashort electronic and nuclear dynamics in excited states [3–9]. In particular, a recent publication by our group demonstrates the power of this methodology to unravel the dynamics of a photodissociation reaction [9], where a visible pump pulse excites IBr molecules onto the $B\,^3\Pi_{0^+}$ electronic state and the nonadiabatic dissociation dynamics is probed by core-to-valence transitions in the XUV. The measured attosecond transient-absorption spectra unravel the photodissociation dynamics and in particular directly observe the wave-packet bifurcation and the electronic character switching at a curve crossing. The aim in the work here is to visualize and quantify the real-time nuclear coherent motion of a molecule, in particular, a broad, highly extended vibrational wave packet created in the bound $B\,^3\Pi_{0^+_u}$ state of the iodine molecule

(I_2). The wave-packet visualization is made possible by taking advantage of the dramatic shift in core-level XUV transition energies with vibrational excitation. In addition, this nuclear coherent motion is used to extract relevant information on the shape of the potential-energy curves of the core-excited electronic states accessed through XUV transitions.

Molecular iodine constitutes a prototype for molecular dynamics from early photodissociation studies to recent XUV-IR experiments [10–12]. Its first absorption band lying between 420 and 800 nm is characterized by minor transitions to the repulsive $A\,^3\Pi_{1_u}$ and $B''\,^1\Pi_{1_u}$ excited states and by a major absorption to the bound $B\,^3\Pi_{0^+_u}$ with an absorption maximum around 530 nm (see Figs. 1 and 2) [13]. We note that, following Mulliken notation, the term associated with the Ω-ω coupling (Hund's case c) is specified as an extra label in the subscript [14]. In early experimental and theoretical work, the weak $A\,^3\Pi_{1_u}$ state was shown to be excited in the red edge (in particular ~650–700 nm) and to undergo direct dissociation while absorption into the minor B'' state was found in the blue edge with an absorption maximum at 490 nm [13,15]. Predissociation from the major B state, characterized by lifetimes on the nanosecond timescale, occur through a crossing with the B'' repulsive state and was extensively investigated [16–20]. Pioneering femtosecond pump-probe experiments were performed by Zewail and co-workers on the vibrational wave-packet dynamics produced by excitation of a few vibrational levels in the B state [10,21–23]. The light-induced fluorescence signal presented characteristic oscillations reflecting vibrational and rotational coherences. The results were analyzed in detail in terms of information extracted on the nuclear vibrational and rotational motion, rotation-vibration coupling, and experimental determination of the potential-energy curve. More recently, two simultaneous

_____

*smarggi@ucm.es
†Present address: Stanford PULSE Institute, SLAC National Accelerator Laboratory, Menlo Park, California 94025, USA.
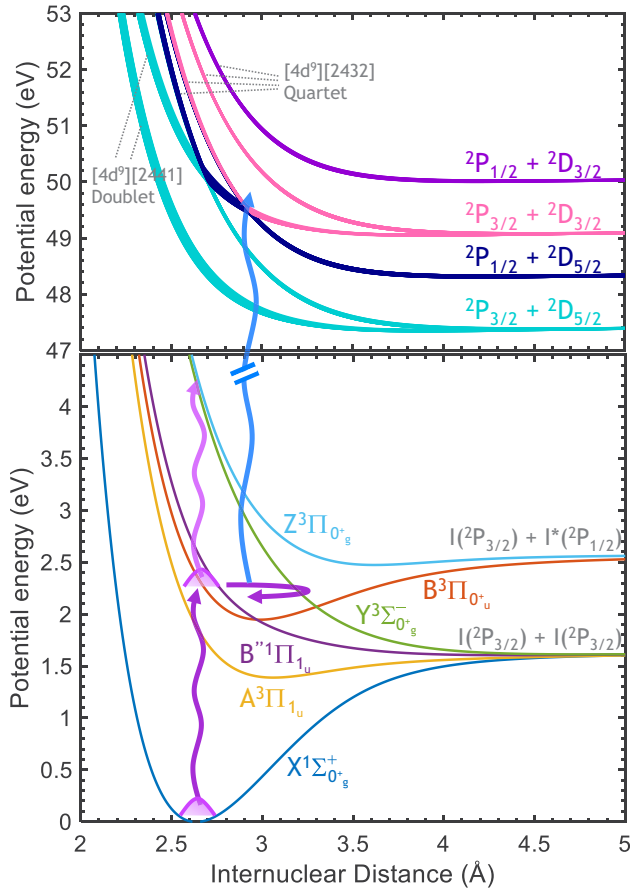‡srl@berkeley.edu

022817-1

FIG. 1. Relevant computed potential-energy curves of I_2, including the first excited valence states populated following one- and two-photon absorption (visible pulse) along with the core-excited states populated by the XUV probe. (See Appendix A for more information on the electronic configuration of the core-excited states.)
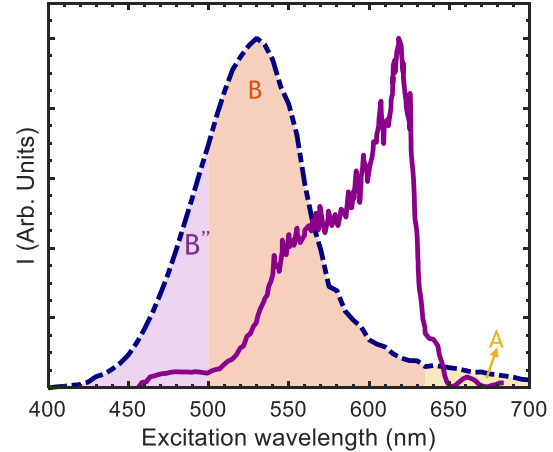

FIG. 2. Absorption spectrum of I_2, in the visible (blue line) compared to the spectrum characterizing the visible pump pulse (purple line). The spectral region where each excited state, $A\,^3\Pi_{1_u}$, $B\,^3\Pi_{0^+_u}$, and $B''\,^1\Pi_{1_u}$, absorbs are highlighted by a yellow, orange, and violet area, respectively.

investigations have imaged the motion of the vibrational wave packet in the B state employing pump-probe x-ray diffraction [24] and ultrafast electron diffraction [25] with a temporal resolution of 30 and 230 fs, respectively. In both cases, analyses of the diffraction data allow the atomic distance as a function of the time delay to be experimentally derived, with a spatial resolution of 0.07 and 0.3 Å, respectively, for x-ray and electron diffraction.

In the present work, we show how attosecond transient XUV spectroscopy permits direct visualization of the coherent nuclear motion with outstanding temporal and spectral resolution, allowing also to directly reconstruct the transition energy as a function of interatomic distance (ranging between 2.7 and 3.8 Å) between the initially populated valence state and the core-excited states accessed by XUV transitions. As illustrated in Fig. 1, a broad vibrational wave packet is created in the B state upon excitation by a 13-fs visible pulse (500–650 nm) and its motion is probed by a time-delayed attosecond XUV pulse (40–70 eV) through XUV transitions into core-excited molecular states, corresponding to the excitation of an electron from an iodine $4d$ orbital ($4d_{5/2}$ or $4d_{3/2}$) into a σ^*, π, or π^* valence orbital (see Appendix A) [26]. These molecular transitions correlate in

the asymptotic limit with well-known atomic transitions, i.e., $I\,^2P_{3/2} \rightarrow\,^2D_{5/2}$(45.9 eV) and $I^*\,^2P_{1/2} \rightarrow\,^2D_{3/2}$(46.7 eV), corresponding to an excitation from a $4d$ orbital into the valence $5p$ orbital. The experimental results are complemented by electronic structure calculations and wave-packet simulations. Computed potential-energy curves for valence and core-excited electronic states are depicted in Fig. 1 and the corresponding absorption probabilities between valence electronic states, in particular $X\,^1\Sigma^+_{0^+_g}$, $B\,^3\Pi_{0^+_u}$, $Y\,^3\Sigma^-_{0^+_g}$, and $Z\,^3\Pi_{0^+_g}$, and the core-excited states are plotted (see Fig. 10, Appendix A). As observed, one-photon visible excitation leads to major population on the $B\,^3\Pi_{0^+_u}$ state and subsequent one-photon excitation from the B state into the repulsive $Y\,^3\Sigma^-_{0^+_g}$ and $Z\,^3\Pi_{0^+_g}$, states is also favorable, as shown in Fig. 1. The absorption transient spectra following excitation at selected wavelengths between 500 and 600 nm have also been simulated by solving the time-dependent Schrödinger equation for the nuclear motion.

II. METHODS

A. Experimental setup

The table-top attosecond transient-absorption apparatus has been previously described in detail [9]. A titanium:sapphire laser system (Femtopower Pro, Femtolasers GmbH) is employed, producing carrier envelope phase-stable near-infrared (NIR) femtosecond pulses centered at 790 nm (1.8 mJ, 1 kHz). The NIR output is focused into a stretched hollow core fiber (1.5 m, 400 μm, Few-cycle Inc.) filled with 1.9 bar of neon for spectral broadening while the resulting pulses are compressed using 12 chirped mirrors (PC 70, Ultrafast Innovations GmbH), a 2-mm-thick ammonium dihydrogen phosphate crystal (United Crystals Inc.), and fused-silica wedges. Few-cycle ∼3.8-fs broadband NIR pulses (0.9 mJ) with a spectrum extending from ∼520 to ∼900 nm are obtained and regularly characterized using a D scan [27,28]. One part (0.3 mJ) is separated using a

broadband beam splitter and used to generate the visible pump pulse by employing two spectral separators for visible light (Layertec GmbH). This visible component of the input pulse, between 500 and 650 nm, is reflected by the separators while the NIR part is transmitted. Another part of the broadband NIR pulses is focused into a quasistatic gas cell filled with argon to produce attosecond XUV pulses (40–70 eV, ∼170 as according to previous streaking measurements [27]) through high harmonic generation while the residual NIR is removed by a 300-nm-thick aluminum filter. The visible pump pulse and the XUV probe pulse are combined at a hole mirror, which are then reflected by a gold-coated toroidal mirror into an absorption gas cell (2-mm path length with entrance and exit pinholes) filled with I_2 vapor. The molecular iodine sample (Sigma-Aldrich, ⩾ 99.8%) is heated at around 65 °C to create an adequate vapor pressure for the transient-absorption measurements. The transmitted spectrum is recorded using a concave grating and an x-ray charge-coupled device (CCD) camera. Well-known Fano resonances of neon between 40 and 50 eV [29] are used for XUV photon energy calibration while time overlap between visible pump and XUV probe pulses is determined by *in situ* measurement of shifts in core-excited helium, obtaining a cross correlation fitted to a Gaussian function and characterized by full width at half maximum (FWHM) of 13.0 ± 0.5 fs, in agreement with previous characterization of the visible pulse using a frequency resolved optical gating (FROG) scan.

B. Theoretical method: Electronic structure

The electronic structure calculations of I_2 are performed by using the spin-orbit general multiconfigurational quasidegenerate perturbation theory (SO-GMC-QDPT) implemented in a developer version of GAMESS US [30–32]. For all calculations, model core potentials with basis sets of triple-zeta quality are used [33,34]. First, a Hartree-Fock calculation at the equilibrium distance of $R_{eq} = 2.63$ Å is carried out, and the output molecular orbitals are used for subsequent multiconfigurational self-consistent field calculations. Two active spaces are defined based on the occupation-restricted-multiple-active-space scheme [35]; a valence-active space consists of 10 electrons distributed in 6 orbitals (i.e., I $5p$ orbitals), and a core-active space consists of 20 electrons distributed in 10 orbitals (i.e., I $4d$ orbitals). The valence space is defined as a complete active space, whereas only single excitations are allowed from the core-active space to the valence-active space, which depicts the $4d \rightarrow 5p$ core-to-valence transitions. In the state averaging, 186 electronic states are included; 36 neutral states (I + I), 30 ionic states ($I^+ + I^-$), and 120 core-excited states ($I^* + I$). To accurately reproduce the spin-orbit couplings for the I $4d$ and I $5p$ shells, an effective nuclear charge of $Z_{eff} = 71.5$ was used and the spin-orbit matrix coupling constant for the I $4d$ shell was scaled down by 42%. In addition, a constant energy shift of $+0.22$ eV has been added to the I $4d$ core states to properly reproduce the experimental energy of the $4d \rightarrow 5p$ transition.
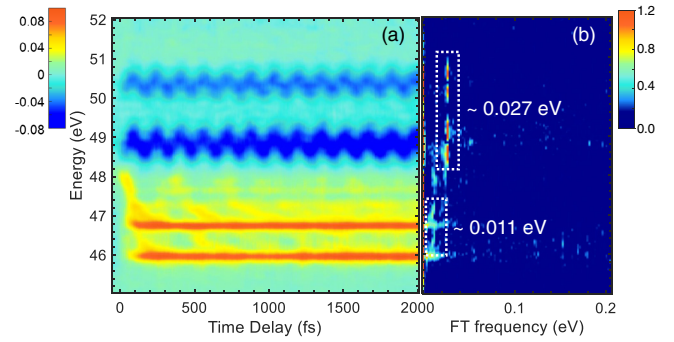

FIG. 3. Measured differential absorption map and Fourier analysis. (a) Measured transient-absorption spectra (in ΔOD) as a function of the time delay and of the XUV photon energy. (b) Fourier transformation along the time-delay abscissa axis of the transient-absorption map in panel (a). White dotted boxes highlight the major frequencies observed.

C. Theoretical method: Dynamics

The molecular dynamics on the $X\ ^1\Sigma_{0^+_g}^+$, $B\ ^3\Pi_{0^+_u}$, $Y\ ^3\Sigma_{0^+_g}^-$ and $Z\ ^3\Pi_{0^+_g}$ states as well as the time-resolved XUV absorption signals therein are simulated by numerically solving the time-dependent Schrödinger equation (TDSE) for the nuclear motion,

$$i\frac{\partial}{\partial t}\boldsymbol{\Psi}(R,t) = \boldsymbol{H}(R,t)\boldsymbol{\Psi}(R,t), \qquad (1)$$

where Ψ is the nuclear wave functions of the valence electronic states. Equations are expressed in atomic units unless otherwise noted. The Hamiltonian for the nuclear motion including the dipole interaction with the visible pump pulse is given by

$$\boldsymbol{H}(R,t) = -\frac{1}{2m}\frac{\partial}{\partial R^2} + \boldsymbol{V}(R) - E_{Vis}(t)\boldsymbol{\mu}(R), \qquad (2)$$

where R is the internuclear distance, V is the potential energies, E_{VIS} is the electric field of the visible pump pulse, and μ represents the transition dipole moments between the valence electronic states. The grid space spans from 2.0 to 7.0 Å with intervals of 0.01 Å, and nuclear wave packets are expressed by the sinc-function discrete variable representation [36]. Complex absorbing potentials are defined at the end of the grid to smoothly eliminate the dissociating components from the $Y\ ^3\Sigma_{0^+_g}^-$ and $Z\ ^3\Pi_{0^+_g}$ states. The visible pump is defined by a 10-fs Gaussian pulse centered at a variable wavelength from 500 to 600 nm. The XUV absorption signals at each delay time are obtained by convoluting the nuclear wave packets with the R-dependent core-to-valence absorption strengths (see Appendix A, Fig. 10), wherein the contributions from different valence states are taken as an incoherent summation.

III. RESULTS AND DISCUSSION

The transient-absorption spectra measured as a function of the time delay between the visible pump and the XUV probe pulse are presented in Fig. 3(a). The time delay, τ, varies from -50 fs to 2 ps with time steps of 10 fs, while at each
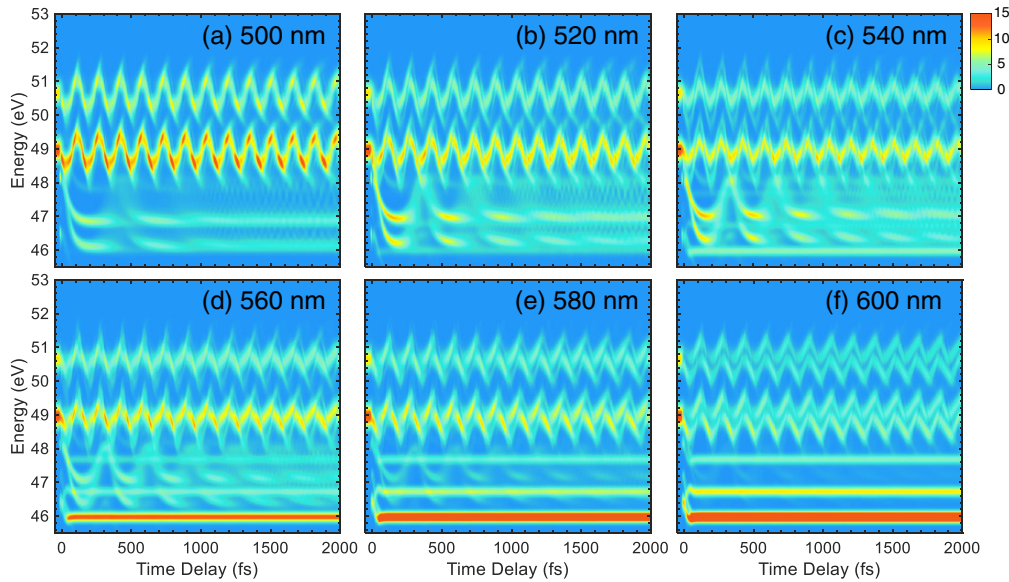
FIG. 4. Simulated absorption maps in terms of absorbance (arb. units) as a function of the XUV photon energy and the time delay. Panels (a) through (e) show results for different visible optical excitation wavelengths.

time delay the pump-probe spectrum $[I_{Vis+XUV}(E_{XUV}, \tau)]$ is collected for 120 frames (100 laser pulses per frame) and the probe pulse-only spectrum $[I_{XUV}(E_{XUV})]$, similarly recorded at each time, is subtracted. In Fig. 3(a), the transients defined as variations in the optical density, $\Delta OD = -\ln[I_{Vis+XUV}(E_{XUV}, \tau)/I_{XUV}(E_{XUV})]$, are plotted as a function of the time delay, τ, and of the XUV photon energy, E_{XUV}, between 45.0 and 52.0 eV. Clear oscillations, characterized by a negative ΔOD, are observed around 48.8 and 50.2 eV, reflecting vibrational coherences produced through ground-state depletion. Taking into account the low power characterizing the visible pulse, such coherences are likely produced through resonant impulsive stimulated Raman scattering. Besides these oscillations, some features shifting in energy as a function of the time delay are observed between 45.9 and 48.0 eV along with two major features lying at 45.9 and 46.7 eV and assigned to atomic iodine, I $^2P_{3/2}$ and I* $^2P_{1/2}$, respectively, arising from fast photodissociation of I_2 within 100 fs (see Appendix B).

The Fourier transform analysis of the measured transient spectra has been performed along the time-delay axis to evaluate the periodic frequencies and is plotted in Fig. 3(b). Two characteristic frequencies are obtained: ~27 meV (±2 meV) at higher photon energies (between 48 and 52 eV) and ~11 meV (±2 meV) at photon energies around 47.2 and 46.5 eV. The former is indeed consistent with the vibrational frequency, $\omega_e = 214.50$ cm^{-1} (26.7 meV) of the I_2 in its ground state while the latter reflects the vibrational motion induced in highly excited levels of the $B\,^3\Pi_{0^+_u}$ state ($\omega_e = 125.69$ cm^{-1}, i.e., 15.6 meV, and $\omega_e \chi_e = 0.764$ cm^{-1} [37]) of I_2.

The simulated XUV absorption spectra including the contributions of the dynamics on all valence states considered in the calculations of the $X\,^1\Sigma^+_{0^+_g}$, $B\,^3\Pi_{0^+_u}$, $Y\,^3\Sigma^-_{0^+_g}$, and $Z\,^3\Pi_{0^+_g}$ states are depicted in Fig. 4 for selected excitation wavelengths between 500 and 600 nm within the experimental

pump pulse employed. Excitation into the B state is negligible for wavelengths above 600 nm as observed in Fig. 1 (see Appendix C).

In contrast to the experimental data measuring a variation in absorption, ΔOD, these simulated maps directly reflect the absorption strength. Well-resolved oscillations around ~48.8 and ~50.2 eV are characterized here by a positive absorbance but give rise to a negative one since they reflect the vibrational coherences produced from the depletion of the ground state. While some oscillatory features lying between 45.9 and 48.0 eV reflecting the vibrational wave packet on the B state are well observed at wavelengths between 520 and 560 nm, at longer wavelengths the two features at 45.9 and 46.7 eV from atomic I and I* are observed due to the major dissociation on the Y and Z states populated through two-photon absorption. At a shorter wavelength, 500 nm, the oscillatory structure from the B state is almost washed out and some dissociation from this state is observed. This dissociation pathway is however rather unfavorable and negligible with respect to the two-photon dissociation at longer wavelengths.

An expanded view of the measured transient-absorption spectra is depicted in Fig. 5(a) for E_{XUV} between 45.5 and 48.2 eV where a number of features are observed that contain information about the induced photodynamics. Besides the two peaks at 45.9 and 46.7 eV corresponding to I $^2P_{3/2}$ and I* $^2P_{1/2}$ formation from dissociation, the time-dependent periodic features reflecting the vibrational motion on the B state are observed in detail now and highlighted in Fig. 5(a) by red arrows. We note that the core-excited states are characterized by two different angular momenta $j = 5/2$ and $j = 3/2$, giving rise to duplicated features: the periodic structures around 47.2 eV, i.e., lying between ~47 and 48 eV are from the $4d_{5/2} \rightarrow \sigma^*$ transition and the other ones, less intense, are from the $4d_{3/2} \rightarrow \sigma^*$ transition, observed between 46.5 and 46.0 eV [26]. The shift in energy as a function of τ characterizing these periodic features mainly reflects the shape of the
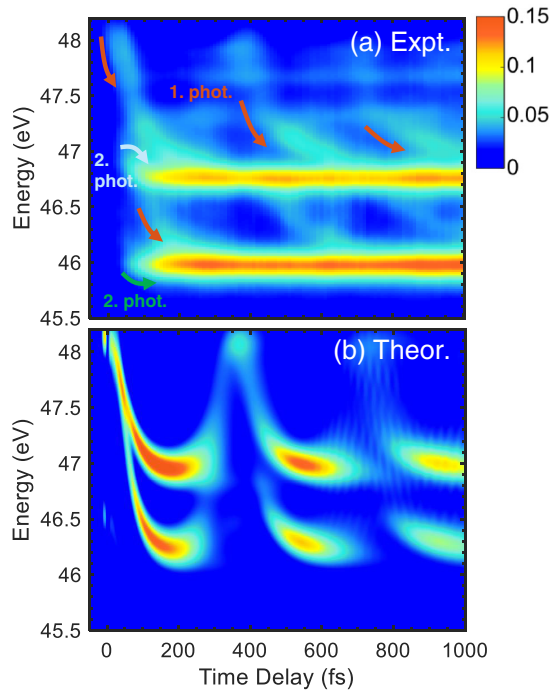
FIG. 5. (a) Experimental transient-absorption map (in ΔOD) following I$_2$ excitation by the visible pump pulse, as a function of the time delay and the XUV photon energy. Red arrows (labeled 1. phot.) highlight the observed vibrational wave-packet motion by one-photon absorption as features significantly moving in energy with time. Green and light cyan arrows (labeled 2. phot.) indicate additional direct dissociation features due to two-photon excitation in the experimental data (see Fig. 6). (b) Simulated transient absorption (1. phot.) from the wave packet in $B\,^3\Pi_{0^+_u}$ excited state following one-photon absorption at 520 nm.

core-excited potentials probed by the XUV pulse as the wave packet moves in the B state.

Vibrational coherences previously observed using transient spectroscopy typically arise from the depletion of the ground state and involve only a few vibrational levels; they are identified as a complete oscillatory feature characteristic of a wave packet that oscillates over a short range of internuclear distances [4–6,38]. In contrast, here a broad distribution of vibrational levels between $v' = 10$ and $v' = 50$ in the B state, with a maximum around $v' = 25$, is created according to the estimated excitation probability based on the visible pump-pulse spectrum and on computed Franck-Condon factors between an assumed initial population on the $X\,^1\Sigma_{0^+_g}$ ($v = 0$, 1, 2) and the B state (see Appendix C). In addition, the broad potential well of the B state allows us to probe a large range of internuclear distances and therefore a large extent of the core-excited state potential versus internuclear distance.

The simulated XUV absorption spectra following one-photon excitation into $B\,^3\Pi_{0^+_u}$ at 520 nm are depicted in Fig. 5(b). Quasi-identical periodic features are observed, reflecting the vibrational wave-packet motion on the B state. As observed in Figs. 5(a) and 5(b), a nonconstant ΔOD characterizes these features. Taking into account the nearly constant absorption probability between the B state and the core-

excited states obtained in the calculations (see Appendix A, Fig. 10), this irregular ΔOD directly reflects the wave-packet broadening due to the anharmonicity of the potential-energy curve, as discussed later.

While the formation of atomic iodine dominates the experimental transients, according to the simulations carried out, dissociation on the B state is not favorable even for the higher excitation energies around 500 nm, as observed in Fig. 4 and in Fig. 5(b). In contrast, two-photon absorption into the $Y\,^3\Sigma_{0^-_g}$ and $Z\,^3\Pi_{0^+_g}$ repulsive states followed by direct fast dissociation is relatively favorable. A strong transition dipole moment for one-photon absorption from the B state into these excited states is indeed obtained (see Appendix A, Fig. 9), as this second transition step corresponds to a strong π-π^* excitation. This fast dissociation is characterized by specific features at short-time delays. The transient-absorption spectra measured for time delays varying between -5 and 80 fs, with time steps of 2 fs, collected for 60 frames (50 laser pulses per frame) are depicted in Fig. 6(a) and are compared to the simulated absorption spectra following excitation at 600 and 520 nm. In addition to the fact that the structure starting at $\sim$48 eV shifts in energy (red arrow), which reflects the vibrational motion on the B state, two other features characterize this temporal region [Fig. 6(a)], both attributed to two-photon visible absorption: a feature lying at $\sim$47 eV and another lying at $\sim$46.5 eV; the latter clearly shifts to lower energies. Resonant two-photon excitation into the Y and Z states occurs only at lower excitation energies (560–600 nm), as reflected in Figs. 6(b) and 6(c). The early-time simulated transient following excitation at 520 nm is dominated by the structure starting at $\sim$48 eV, which reflects the vibrational motion on the B state, while two different features, in agreement with the additional structures observed in the experimental map, arise at 600 nm in the calculations. Dissociation on the Y state leads exclusively to the formation of I $^2P_{3/2}$ and is characterized by the feature starting at $\sim$46.5 eV; it shifts in energy as τ increases, which reflects the evolution of the wave packet on the repulsive potential, and reaches the I $^2P_{3/2}$ atomic line at 45.9 eV within 100 fs [green arrows, Figs. 6(a) and 6(b)]. In contrast, dissociation on the Z state is associated with the formation of I $^2P_{3/2}$ + I*$^2P_{1/2}$, distinguished in the simulated transient by the two features crossing (cyan arrows). Although less clearly observed in the experimental map, this dissociation pathway is accordingly assigned to the feature lying around 47 eV. The corresponding transients for I $^2P_{3/2}$ and I* $^2P_{1/2}$ are included in Appendix B (see Fig. 11).

In order to gain a deeper insight into the core-excited electronic states based on the vibrational motion on the B state monitored through transient spectroscopy, the XUV energy position corresponding to the maximum ΔOD in Fig. 5(a) (red arrows) is extracted as a function of τ and plotted in Fig. 7(a). This result is compared to a one-dimensional classical dynamics simulation carried out on the B state (see Appendix C) shown in Fig. 7(b), where the internuclear distance, R, oscillates periodically with τ. A coherent vibrational wave packet is created upon visible one-photon excitation. This wave packet is initially located close to the inner turning point due to the different equilibrium distance characterizing the ground state and the B state ($R_{\mathrm{eq}} = 2.67$ Å vs $R_{\mathrm{eq}} = 3.02$ Å, respectively). While the wave packet evolves in the
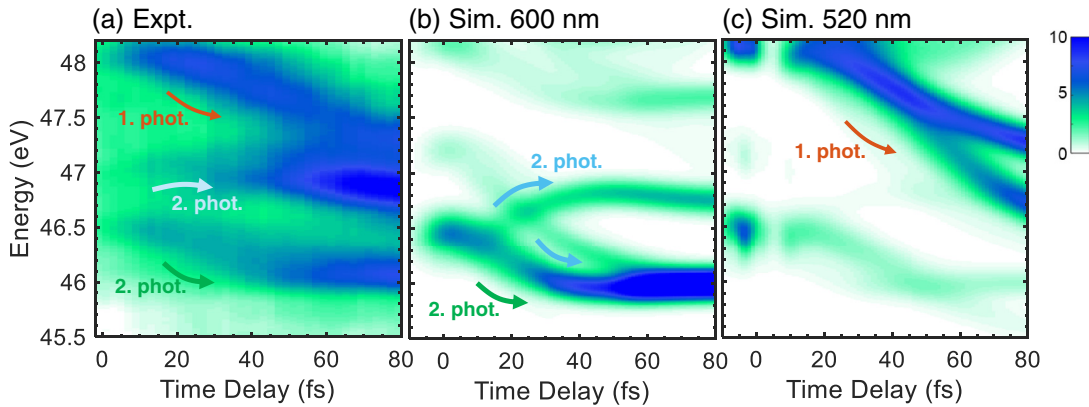
FIG. 6. (a) Experimental transient-absorption spectra (in ΔOD) as a function of the time delay and the XUV photon energy measured for short-time delays, labeled with one- and two-photon arrows. (b), (c) Simulated absorption spectra following excitation at 600 and 520 nm. One-photon vibrational dynamics on the $B\,^3\Pi_{0^+_u}$ state is indicated by red arrows while dissociation dynamics following two-photon absorption into the $Y\,^3\Sigma^-_{0^+_g}$ state is highlighted by green arrows and the corresponding dissociation dynamics from the $Z\,^3\Pi_{0^+_g}$ state is shown by cyan (or light cyan) arrows.

B state as the internuclear distance R increases, the corresponding feature shifts to lower XUV photon energies mainly reflecting the shape of the core-excited potential-energy curve. At $\tau \approx 200$ fs, the vibrational wave packet is located at larger internuclear distances, close to the outer turning point (R around 3.7 Å), and the XUV absorbance signal is large. Taking into account the anharmonic shape of the potential-energy
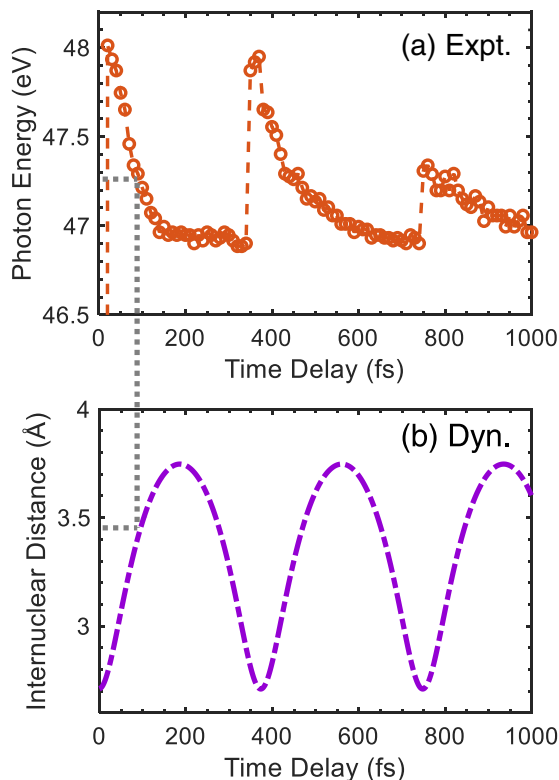

FIG. 7. (a) Photon energy position at the maximum ΔOD of the feature reflecting the vibrational dynamics in the $B\,^3\Pi_{0^+_u}$ state observed in Fig. 2. (b) One-dimension classical dynamics simulation in the $B\,^3\Pi_{0^+_u}$ excited state.

curve (see Fig. 1), the wave packet is considerably broadened at this point, covering a large range of R, but with a range of similar XUV energies. The wave packet is considerably spread when it starts to turn back to smaller R as reflected by both the experimental and the simulated absorption map in Figs. 5(a) and 5(b), respectively. This spreading leads indeed to the decreased absorbance observed in the simulated transients [Fig. 5(b)] while the feature disappears completely in the experiment, as observed in Fig. 5(a). As the wave packet gets close to the inner turning point around $\tau \approx 390$ fs, some recompression of the wave packet occurs due to the sharp shape of the potential at shorter R, as revealed by the appearance of a sharp absorption feature around $\tau \approx 390$ fs. A strong signal enhancement is again observed at later times as the feature shifts to lower energy between $\tau \approx 450$ fs and $\tau \approx 600$ fs when the wave packet gets close to the outer turning point. This behavior, characterized by an increased and decreased spectral dispersion, as the wave packet evolves between the outer and inner turning points has been previously reported [39] and is indeed well observed in the nuclear wave-packet evolution as a function of the time delay as depicted (see Appendix C, Fig. 13). A partial recompression of the wave packet is produced each time the wave packet gets to the inner turning point at shorter R while the wave-packet spreading on the way to or from the outer turning point produces a considerable decrease in signal. After a few oscillations, the feature characterizing the motion on the B state is almost indiscernible for $\tau \geqslant 1000$ fs, reflecting the dephasing of the wave packet due to the anharmonicity of the potential.

The comparison between the XUV absorption energies and the classical dynamics plotted in Fig. 7 allows us to assign, at each time delay, a core-to-valence transition energy to an internuclear distance, hence directly mapping the core-excited states. The results obtained for the absorption feature between 48 and 47 eV ($4d_{5/2} \rightarrow \sigma^*$) are depicted in Fig. 8 overlaid with the computed transition probability between the valence B state and the core-excited states, showing excellent agreement. The same mapping is performed for the shifting feature arising at 46.5–46.0 eV ($4d_{3/2} \rightarrow \sigma^*$), although over a narrower region of R, and the result is shown in Fig. 8. By
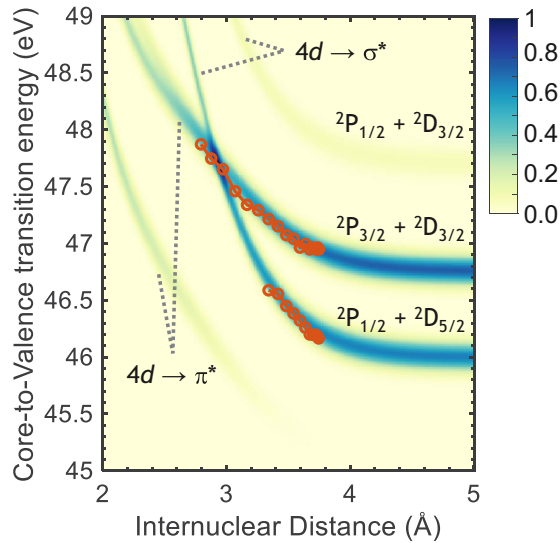
FIG. 8. Computed XUV absorption strengths from the $B\,^3\Pi_{0^+_u}$ state into the core-excited states as a function of the transition energy and the internuclear distance. The color scale shows the normalized transition probability. Orange circles and orange lines: experimental curve of core-level transition energy versus internuclear separation extracted from the experimental transient-absorption map.

creating a vibrational wave packet on the B state, we directly probe the transition energy between the B state and the core-excited states, obtaining valuable information on the shape of the potential of the latter. In addition, the wide potential well characteristic of the B state permits a mapping of a large portion of the core-excited state potential versus internuclear separation. The shape of such core-excited states can be understood in diatomic molecules by the equivalent core model, which assumes that removing a core electron is, for the outer electrons, equivalent to an increase in the nuclear charge by one unit. In this picture, the first resonant state is equivalent to the xenon iodide (XeI) ground state. Its potential-energy curve is weakly bound ($D_e \sim 33$ meV) due to a van der Waals attraction and presents indeed an overall repulsive shape [40]. In contrast, potential-energy curves of core-excited states in larger polyatomic molecules are often not well known and the present work opens the door for their experimental determination.

IV. CONCLUSION

Attosecond XUV transient-absorption spectroscopy is employed to image coherent nuclear motion in real time. One-photon visible pump absorption is employed to create a broad vibrational wave packet in the valence-excited $B\,^3\Pi_{0^+_u}$ state of I_2 while the dynamics are probed by core-to-valence transitions through one-photon XUV absorption. The vibrational motion in the B state is directly observed in real time for more than one picosecond, in excellent agreement with simulated absorption maps, while concurrent two-photon absorption and subsequent fast direct dissociation, within 100 fs, is discerned and discussed. In contrast to traditional reported vibrational coherences involving a few vibrational levels and often lasting many picoseconds, by one-photon

absorption a broad vibrational wave packet in the B state is created here, from $v' = 10$ to $v' = 50$ with a maximum around $v' = 25$, and its motion is directly visualized in the XUV transient spectra as a characteristic feature shifting in energy. The wave-packet spreading at the outer turning point and the later recompression at the inner turning point is clearly observed in agreement with the simulated absorption maps, while after a few oscillations the anharmonicity of the potential-energy curve leads to the dephasing of the wave packet for $\tau \geqslant 1000$ fs. In contrast to the present work, previous reports of coherent nuclear motion on the B state employing in particular ultrafast electron diffraction [25] and x-ray diffraction [24] involved only a few vibrational levels ~ 5. Moreover, the wave-packet evolution including its increased and decreased spectral dispersion at the outer and inner turning points was not observed before. In both Refs. [23,25], further analysis was also required to derive the internuclear distance as a function of the time delay. Although XUV transient-absorption spectroscopy does not allow us to directly determine accurate geometrical information, it constitutes an ideal tool to unravel vibrational motion as a result of its unique spectral and temporal resolution. In addition, the observed shifting in energy associated with the vibrational motion in the B states reflects the transition energy between the valence and the core-excited states as a function of the internuclear distance. It gives thus direct information on the potential-energy curves of the core-excited states. The transition energy between the valence B state and the core-excited states as a function of the internuclear distance (ranging between 2.7 and 3.8 Å) is indeed experimentally derived by combining attosecond transient absorption spectroscopy experimental results with a simple one-dimensional classical calculation. Such information can be of particular interest in larger molecules, where *ab initio* calculations of core-excited states are particularly demanding.

APPENDIX A: ELECTRONIC STRUCTURE CALCULATIONS AND SIMULATED ABSORPTION SPECTRA USING THE SO-GMC-QDPT CODE

The transition dipole moments (TDMs) computed as a function of the internuclear distance R for one-photon excitation from the I_2 ground state into $A\,^3\Pi_{1_u}$, $B''\,^1\Pi_{1_u}$, and $B\,^3\Pi_{0^+_u}$ excited states are depicted in Fig. 9. The one-photon excitation of the B state is clearly favored at $R_{eq} = 2.63$ Å while absorption into the A and B'' states can be considered as negligible. In contrast, further two-photon dynamics cannot be ruled out. As observed in Fig. 9(b), a large transition dipole
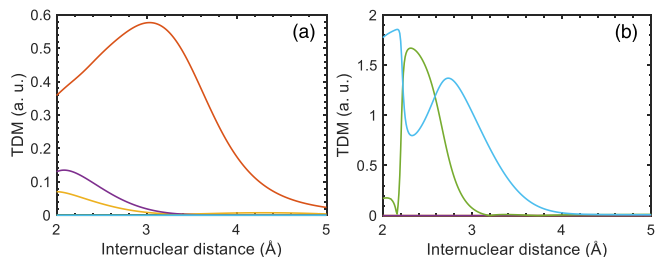
FIG. 9. Computed transition dipole moments (TDM) (a) as a function of the internuclear distance R for one-photon excitation from the I_2 ground state into $A\,^3\Pi_{1_u}$ (yellow line), $B''\,^1\Pi_{1_u}$ (purple) and $B\,^3\Pi_{0^+_u}$ (red line) excited states, and (b) TDM for one-photon excitation from the populated $B\,^3\Pi_{0^+_u}$ state into the $Y\,^3\sum_{0^+_g}^-$ (green line) and $Z\,^3\Pi_{0^+_g}$ (cyan) excited states.

moment is observed for one-photon excitation from the B state into the repulsive Y and Z states.

Since Λ and Σ are not good quantum numbers for this molecule, which is better described by the Ω-ω coupling (Hund's case c), the term associated with the Ω-ω coupling is specified as an extra label in subscript. While $A\,^3\Pi_{1_u}$, $B\,^3\Pi_{0^+_u}$, and $B''\,^1\Pi_{1_u}$ excited states have been well reported in experimental and theoretical studies, the $Y\,^3\Sigma_{0^+_g}^-$ and $Z\,^3\Pi_{0^+_g}$ excited states have been identified based on theoretical work

[14,41] and to the best of our knowledge have not been observed experimentally.

The combination of the two iodine atoms with a configuration $5s^25p^5\,^2P$ leads to molecular states characterized by the electronic configuration $\sigma_g^2\sigma_u^2\sigma_g^m\pi_u^p\pi_g^q\sigma_u^n$. The different electronic states are therefore denoted as [mqpn]. In particular, the ground state is described as a [2440] configuration, while valence excited states $A\,^3\Pi_{1_u}$, $B''\,^1\Pi_{1_u}$, and $B\,^3\Pi_{0^+_u}$ correspond to a [2431] configuration. The transition from the ground state into the B state corresponds therefore to a $\pi^* \rightarrow \sigma^*$ excitation. Finally, the upper states, defined in the calculations as two 0^+_g states and attributed to the $Y\,^3\Sigma_{0^+_g}^-$ and $Z\,^3\Pi_{0^+_g}$ excited states based in particular on Mulliken's work [14] are characterized by a [2341] and a [2422] configuration, respectively. The configuration interaction coefficients as a function of the internuclear distance describing these two states are however strongly mixed as previously observed for IBr and ICl molecules [42] and their configuration is expected to change through avoided crossings and at the asymptotic limit. Thus, both excited states can be described to some extent as a [2341] configuration and their population from the B state is associated with a global $\pi \rightarrow \pi^*$ excitation. We note that core-excited states of an electronic configuration $[4d^{-1}][2441]$, $[4d^{-1}][2432]$, $[4d^{-1}][2342]$, and $[4d^{-1}][1442]$, are included in the calculations to simulate the core-to-valence electronic transition $4d \rightarrow \sigma^*$, π or π^* used to probe the dynamics. The computed absorption probabilities between
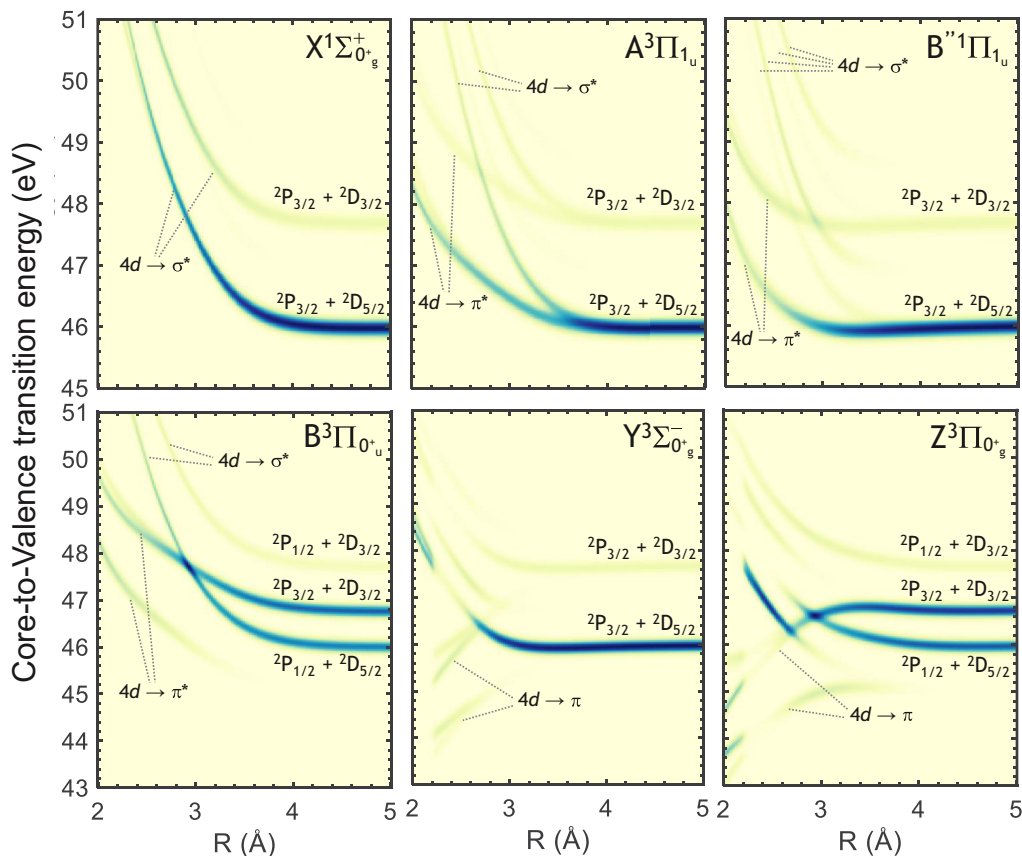

FIG. 10. Computed absorption probabilities between each valence electronic state and the core-hole excited states as a function of the core-to-valence transition energy and the internuclear distance R.
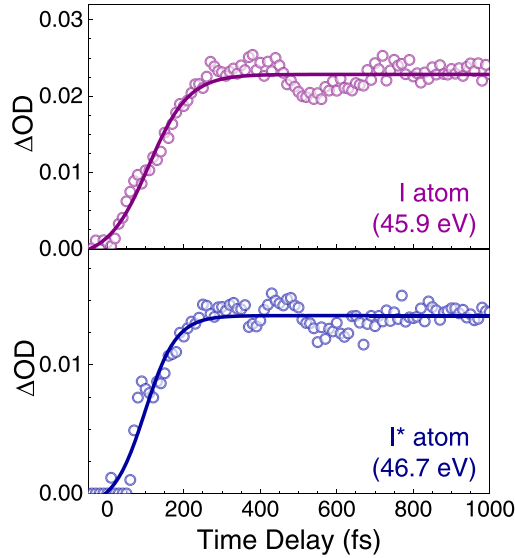
FIG. 11. Measured transient for the dissociation into I and I* atomic fragments. Time traces extracted from Fig. 5(a): Amplitude of the Gaussian's functions (circles) used to describe the features associated with the formation of I and I* at around 45.9 and 46.7 eV, as a function of time, and the corresponding fit to a Boltzmann sigmoidal function (line). Both transients are consistent with a fast dissociation with $\tau_{diss} \sim 100$ fs.

the valence electronic states and the core-excited states are depicted in Fig. 10.

APPENDIX B: EXTRACTED I AND I* TIME TRACES

The transient spectra at each time delay from the map shown in Fig. 5(a) were fitted using two narrow Gaussian functions (fixed width ~0.15 eV) to describe the two features assigned to the formation of atomic I and I*, and two broad Gaussian functions (fixed width and position) to describe the underlying *background* (containing the shifting feature reflecting the motion on the *B* state). This procedure allows us to properly extract the time traces describing the iodine dissociation (see Fig. 11) as the amplitude of two corresponding narrow Gaussian functions as a function of the time delay. In addition, these two dissociation channels can be subtracted from the experimental map in order to properly extract the position of the maximum ΔOD characterizing the shifting feature from the vibrational motion on the *B* state (see Fig. 5 (a) and Fig. 7).

APPENDIX C: EXCITATION PROBABILITY AND CLASSICAL DYNAMICS

The excitation probability has been estimated based on the visible pump-pulse spectrum and on computed Franck-Condon factors between the initially populated $X\ ^1\Sigma_{0^+_g}^+$ and the *B* state. Morse potentials from spectroscopic measurements [43–45] have been considered for both the $X\ ^1\Sigma_{0^+_g}^+$ and the $B\ ^3\Pi_{0^+_u}$ states (see Table I). Vibrational wave functions of each electronic state were obtained by the diagonalization of the Hamiltonian (through the finite elements method using

TABLE I. Morse parameters characterizing the potential-energy curves for the *X* and *B* states of I_2 (from Refs. [43–45])

	D_e (cm^{-1})	ω_e (cm^{-1})	R_{eq} (Å)
X state	12 439.4	214.5	2.666 3
B state	5 168.14	125.69	3.024 7

70 solutions). The computed Franck-Condon factors are then weighted by the experimental pump-pulse spectrum to obtain the excitation probability.

The Franck-Condon factors, depicted in Fig. 12, were calculated for three different initial vibrational populations: considering an initial $v = 0$ population only, a small fraction in $v = 1(0.2)$, with 0.8 in $v = 0$, and a small fraction in both $v = 1(0.2)$ and $v = 2(0.1)$, with 0.7 in $v = 0$. The corresponding excitation probability for the three initial conditions is plotted in Fig. 12(b). Although a major initial population on $v = 0$ is expected, we cannot rule out some population of $v = 1$ and $v = 2$ since the inlet system to the cell is heated at 65 °C. As observed, the vibrational wave packet created is not significantly dependent on the initial vibrational population on the ground state. In all cases, the excitation probability shows a maximum around $v' = 25$, ranging from approximately $v' =$
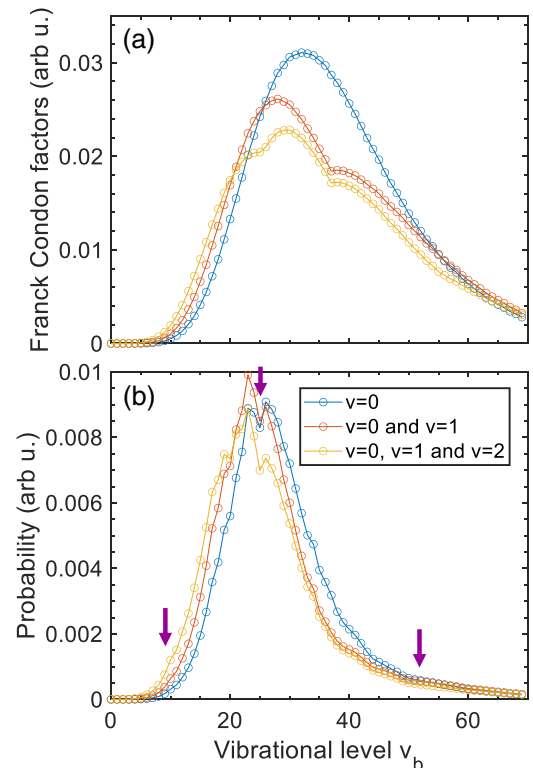

FIG. 12. (a) Computed Franck Condon factors between the ground state and the $B\ ^3\Pi_{0^+_u}$ state as a function of the populated vibrational level on the *B* state. Three initial vibrational populations in the *X* state are considered: only $v = 0$, $v = 0$ (80%), and $v = 1$ (20%), and $v = 0$ (70%), $v = 1$ (20%) and $v = 2$ (10%). (b) Corresponding excitation probability using the pump-pulse spectrum. Vertical purple arrows indicate the three starting points selected for the classical dynamics [Fig. 13(b)].
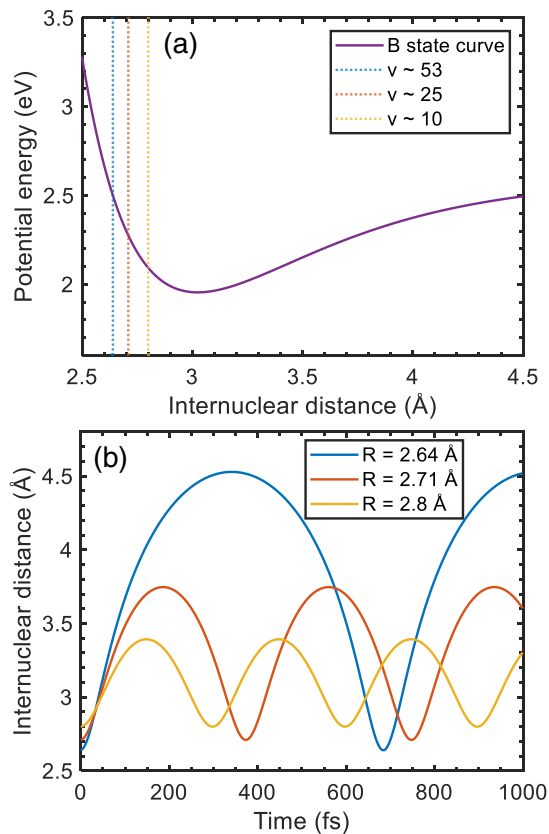
FIG. 14. Nuclear wave-packet evolution (color map) in the *B* state, following excitation at 520 nm (obtained by numerically solving the TDSE for the nuclear motion) compared with the one-dimension classical dynamics (orange line).

FIG. 13. (a) Morse potential characterizing the *B* state. Vertical lines indicate the three selected starting points, defined by the corresponding R_i distance, and associated with the intensity maxima of the excitation probability ($v' = 25$, orange line) as well as the lower (yellow) and higher (blue) vibrational levels populated. (b) Evolution of the internuclear distance as a function of time, resulting from the dynamics carried out in the *B* state. Three starting points are considered as indicated in panel (a).

10 to $v' = 50$, which correspond to an excitation wavelength from ~600 to ~500 nm.

One-dimensional classical molecular-dynamics simulations were performed in the Morse potential characterizing the *B* state. The dynami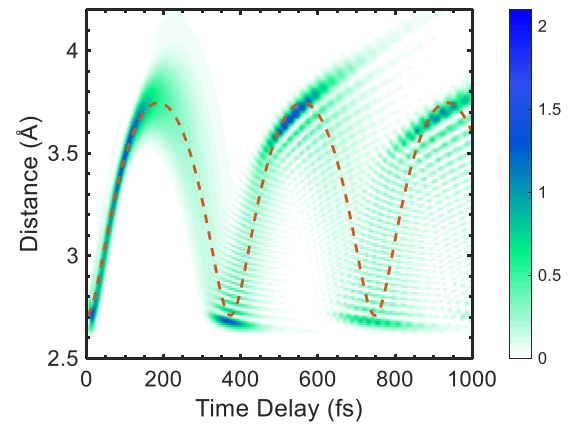cs are started at selected internuclear distances, within the Franck-Condon region associated with the I_2 ground state. The initial internuclear distances R_i are selected based on the computed excitation probability. The dynamics is carried out for the R_i associated with the intensity maxima at around $v' = 25$ as well as with the lower and higher vibrational levels populated around $v' = 10$ and close to $v' = 50$. The results are depicted in Fig. 13. Oscillations of R whose frequency strongly depends on the v' level are observed characterizing the dynamics on the *B* state. The dynamics obtained for the intensity maxima at around $v' = 25$ is consistent with the experimental results. The classical dynamics simulation is compared in Fig. 14 to nuclear wave-packet evolution obtained by numerically solving the TDSE for the nuclear coordinates, which was performed within the calculations to simulate the transient-absorption spectra. As expected, an excellent agreement is observed. While molecular dynamics obtained by solving the TDSE gives considerably more information, although requiring a bigger effort, a simple one-dimensional classical dynamics simulation permits us to extract the evolution of the internuclear distance as a function of time.

[1] S. Biswas, B. Förg, L. Ortmann, J. Schötz, W. Schweinberger, T. Zimmermann, L. Pi, D. Baykusheva, H. A. Masood, I. Liontos, A. M. Kamal, N. G. Kling, A. F. Alharbi, M. Alharbi, A. M. Azzeer, G. Hartmann, H. J. Wörner, A. S. Landsman, and M. F. Kling, Probing molecular environment through photoemission delays, Nat. Phys. **16**, 778 (2020).

[2] P. M. Kraus, B. Mignolet, D. Baykusheva, A. Rupenyan, L. Horný, E. F. Penka, G. Grassi, O. I. Tolstikhin, J. Schneider, F. Jensen, L. B. Madsen, A. D. Bandrauk, F. Remacle, and H. J. Wörner, Measurement and laser control of attosecond charge migration in ionized iodoacetylene, Science **350**, 790 (2015).

[3] E. Goulielmakis, Z.-H. Loh, A. Wirth, R. Santra, N. Rohringer, V. S. Yakovlev, S. Zherebtsov, T. Pfeifer, A. M. Azzeer, M. F.

Kling, S. R. Leone, and F. Krausz, Real-time observation of valence electron motion, Nature (London) **466**, 7307 (2010).

[4] Z. Wei, J. Li, L. Wang, S. T. See, M. H. Jhon, Y. Zhang, F. Shi, M. Yang, and Z.-H. Loh, Elucidating the origins of multimode vibrational coherences of polyatomic molecules induced by intense laser fields, Nat. Commun. **8**, 735 (2017).

[5] Z. Wei, J. Li, S. T. See, and Z.-H. Loh, Spin–orbit state-selective C–I dissociation dynamics of the CH3I+ $\tilde{X}$ electronic state induced by intense few-cycle laser fields, J. Phys. Chem. Lett. **8**, 6067 (2017).

[6] H. Timmers, X. Zhu, Z. Li, Y. Kobayashi, M. Sabbar, M. Hollstein, M. Reduzzi, T. J. Martínez, D. M. Neumark, and S. R. Leone, Disentangling conical intersection and coherent molecular dynamics in methyl bromide with

attosecond transient absorption spectroscopy, Nat. Commun. **10**, 3133 (2019).

[7] L. Drescher, G. Reitsma, T. Witting, S. Patchkovskii, J. Mikosch, and M. J. J. Vrakking, State-resolved probing of attosecond timescale molecular dipoles, J. Phys. Chem. Lett. **10**, 265 (2019).

[8] Y. Pertot, C. Schmidt, M. Matthews, A. Chauvet, M. Huppert, V. Svoboda, A. von Conta, A. Tehlar, D. Baykusheva, J.-P. Wolf, and H. J. Wörner, Time-resolved x-ray absorption spectroscopy with a water window high-harmonic source, Science **355**, 264 (2017).

[9] Y. Kobayashi, K. F. Chang, T. Zeng, D. M. Neumark, and S. R. Leone, Direct mapping of curve-crossing dynamics in IBr by attosecond transient absorption spectroscopy, Science **365**, 79 (2019).

[10] M. Dantus, R. M. Bowman, and A. H. Zewail, Femtosecond laser observations of molecular vibration and rotation, Nature (London) **343**, 6260 (1990).

[11] M. Krikunova, T. Maltezopoulos, P. Wessels, M. Schlie, A. Azima, M. Wieland, and M. Drescher, Ultrafast photofragmentation dynamics of molecular iodine driven with timed XUV and near-infrared light pulses, J. Chem. Phys. **134**, 024313 (2011).

[12] P. H. Bucksbaum, M. R. Ware, A. Natan, J. P. Cryan, and J. M. Glownia, Characterizing Multiphoton Excitation using Time-Resolved X-Ray Scattering, Phys. Rev. X **10**, 011065 (2020).

[13] J. Tellinghuisen, Transition strengths in the visible–infrared absorption spectrum of I2, J. Chem. Phys. **76**, 4736 (1982).

[14] R. S. Mulliken, Iodine revisited, J. Chem. Phys. **55**, 288 (1971).

[15] J. Tellinghuisen, Resolution of the visible-infrared absorption spectrum of I_2 into three contributing transitions, J. Chem. Phys. **58**, 2821 (1973).

[16] M. Broyer, J. Vigué, and J. C. Lehmann, Direct evidence of the natural predissociation of the $I_2 B$ state through systematic measurements of lifetimes, J. Chem. Phys. **63**, 5428 (1975).

[17] L. Brewer and J. Tellinghuisen, Quantum yield for unimolecular dissociation of I_2 in visible absorption, J. Chem. Phys. **56**, 3929 (1972).

[18] J. Vigue, M. Broyer, and J.-C. Lehmann, Predissociation effects in the B $^3\Pi_{0+_u}$ state of iodine, J. Chem. Phys. **62**, 4941 (1975).

[19] G. A. Capelle and H. P. Broida, Lifetimes and quenching cross sections of $I_2(B ^3\Pi_{Ou}^+)$, J. Chem. Phys. **58**, 4212 (1973).

[20] J. Tellinghuisen, Spontaneous predissociation in I_2, J. Chem. Phys. **57**, 2397 (1972).

[21] R. M. Bowman, M. Dantus, and A. H. Zewail, Femtosecond transition-state spectroscopy of iodine: From strongly bound to repulsive surface dynamics, Chem. Phys. Lett. **161**, 297 (1989).

[22] M. Gruebele, G. Roberts, M. Dantus, R. M. Bowman, and A. H. Zewail, Femtosecond temporal spectroscopy and direct inversion to the potential: Application to iodine, Chem. Phys. Lett. **166**, 459 (1990).

[23] M. Gruebele and A. H. Zewail, Femtosecond wave packet spectroscopy: Coherences, the potential, and structural determination, J. Chem. Phys. **98**, 883 (1993).

[24] J. M. Glownia, A. Natan, J. P. Cryan, R. Hartsock, M. Kozina, M. P. Minitti, S. Nelson, J. Robinson, T. Sato, T. van Driel *et al.*, Self-Referenced Coherent Diffraction X-Ray Movie of Angstrom- and Femtosecond-Scale Atomic Motion, Phys. Rev. Lett. **117**, 153003 (2016).

[25] J. Yang, M. Guehr, X. Shen, R. Li, T. Vecchione, R. Coffee, J. Corbett, A. Fry, N. Hartmann, C. Hast *et al.*, Diffractive Imaging of Coherent Nuclear Motion in Isolated Molecules, Phys. Rev. Lett. **117**, 153002 (2016).

[26] F. J. Comes, U. Nielsen, and W. H. E. Schwarz, Inner electron excitation of iodine in the gaseous and solid phase, J. Chem. Phys. **58**, 2230 (1973).

[27] H. Timmers, Y. Kobayashi, K. F. Chang, M. Reduzzi, D. M. Neumark, and S. R. Leone, Generating high-contrast, near single-cycle waveforms with third-order dispersion compensation, Opt. Lett. **42**, 811 (2017).

[28] F. Silva, M. Miranda, B. Alonso, J. Rauschenberger, V. Pervak, and H. Crespo, Simultaneous compression, characterization and phase stabilization of GW-level 1.4 cycle VIS-NIR femtosecond pulses using a single dispersion-scan setup, Opt. Express **22**, 10181 (2014).

[29] K. Codling, R. P. Madden, and D. L. Ederer, Resonances in the photo-ionization continuum of Ne I (20-150 EV), Phys. Rev. **155**, 26 (1967).

[30] M. W. Schmidt, K. K. Baldridge, J. A. Boatz, S. T. Elbert, M. S. Gordon, J. H. Jensen, S. Koseki, N. Matsunaga, K. A. Nguyen, S. Su, T. L. Windus, M. Dupuis, and J. A. Montgomery, Jr., General atomic and molecular electronic structure system, J. Comput. Chem. **14**, 1347 (1993).

[31] T. Zeng, A diabatization protocol that includes spin-orbit coupling, J. Chem. Phys. **146**, 144103 (2017).

[32] Y. Kobayashi, T. Zeng, D. M. Neumark, and S. R. Leone, Ab initio investigation of Br-3 d core-excited states in HBr and HBr+ toward XUV probing of photochemical dynamics, Struct. Dyn. **6**, 014101 (2019).

[33] E. Miyoshi, Y. Sakai, K. Tanaka, and M. Masamura, Relativistic Dsp-model core potentials for main group elements in the fourth, fifth and sixth row and their applications, J. Mol. Struct. THEOCHEM **451**, 73 (1998).

[34] M. Sekiya, T. Noro, Y. Osanai, and T. Koga, Contracted polarization functions for the atoms Ca, Ga–Kr, Sr, and In–Xe, Theor. Chem. Acc. **106**, 297 (2001).

[35] J. Ivanic, Direct configuration interaction and multiconfigurational self-consistent-field method for multiple active spaces with variable occupations. I. method, J. Chem. Phys. **119**, 9364 (2003).

[36] D. T. Colbert and W. H. Miller, A novel discrete variable representation for quantum mechanical reactive scattering via the S-matrix kohn method, J. Chem. Phys. **96**, 1982 (1992).

[37] K. P. Huber and G. Herzberg, Constants of Diatomic Molecules, in *Molecular Spectra and Molecular Structure: IV. Constants of Diatomic Molecules*, edited by K. P. Huber and G. Herzberg (Springer US, Boston, MA, 1979), pp. 8–689.

[38] Z. Wei, J. Li, H. Zhang, Y. Lu, M. Yang, and Z.-H. Loh, Ultrafast dissociative ionization and large-amplitude vibrational wave packet dynamics of strong-field-ionized di-iodomethane, J. Chem. Phys. **151**, 214308 (2019).

[39] T. h. Ergler, A. Rudenko, B. Feuerstein, K. Zrost, C. D. Schröter, R. Moshammer, and J. Ullrich, Spatiotemporal Imaging of Ultrafast Molecular Motion: Collapse and Revival of the D2 Nuclear Wave Packet, Phys. Rev. Lett. **97**, 193001 (2006).

[40] G. J. Hoffman, Ab initio potentials for states of XeI, XeI- and XeI+, Chem. Phys. **361**, 68 (2009).

[41] C. Teichteil and M. Pelissier, Relativistic calculations of excited states of molecular iodine, Chem. Phys. **180**, 1 (1994).

[42] T. Matsuoka and S. Yabushita, Quantum interference effects theoretically found in the photodissociation processes of the second absorption bands of ICl and IBr molecules, J. Phys. Chem. A **119**, 9609 (2015).

[43] B. Amstrup, R. J. Carlson, A. Matro, and S. A. Rice, Use of pulse shaping to control the photodissociation of a diatomic molecule: Preventing the best from being the enemy of the good, J. Phys. Chem. **95**, 8019 (1991).

[44] R. J. LeRoy, Molecular constants and internuclear potential of ground-state molecular iodine, J. Chem. Phys. **52**, 2683 (1970).

[45] P. Luc, Molecular constants and dunham expansion parameters describing the B-X system of the iodine molecule, J. Mol. Spectrosc. **80**, 41 (1980).